Journal of Materials Chemistry A

ROYAL SOCIETY OF CHEMISTRY

PAPER

View Article Online
View Journal

Cite this: DOI: 10.1039/d5ta03658e

PEIE-mediated strategies for highly efficient and stable perovskite solar cells overcoming BCP thermal aggregation†

Hao Xiong, [a] Bowen Li,[a] Hongjie Qiu,[a] Pengfei Liu,[a] Kunyuan Zheng,[b] Zening Lei,[a] Peng Xiang*[a] and Xinyu Tan*[b]

Perovskite solar cells (PSCs) have attracted considerable research interest in recent decades due to their remarkable power conversion efficiencies. However, their thermal stability remains one of the crucial challenges for commercial applications. Bathocuproine (BCP), widely employed as an interfacial buffer layer between the electron transport layer and the metal electrode, tends to undergo thermal aggregation at elevated temperatures, thereby compromising device stability. In this paper, the aggregation behavior of BCP under thermal stability testing was investigated. It was proposed that introducing polyethylenimine ethoxylated (PEIE) into BCP could inhibit its high-temperature aggregation. The –NH and –OH groups in PEIE can form hydrogen bonds with the pyridine nitrogen in BCP. This interaction enables moderate π–π stacking to persist over a broader temperature range, thereby improving morphology and uniformity of the film. Concurrently, PEIE optimizes energy level alignment at the C_{60}/BCP interface, facilitating more efficient electron extraction and transport. Moreover, the incorporation of PEIE remarkably suppresses the infiltration of Ag ions under continuous thermal conditions, which further enhances the thermal stability of the device. By utilizing the PEIE-modified BCP buffer layer, the resulting PSCs demonstrate a champion power conversion efficiency (PCE) of 25.81%. Even after 1000 hours of operation under a relative humidity of 30%, they still retain an efficiency of more than 85%, demonstrating significantly enhanced stability. This work presents an innovative design strategy for developing PSCs with simultaneously enhanced efficiency and operational stability.

Received 8th May 2025
Accepted 18th July 2025

DOI: 10.1039/d5ta03658e

rsc.li/materials-a

1. Introduction

Perovskite solar cells have demonstrated remarkable progress in power conversion efficiency, recently achieving a certified record efficiency of 26.70%.[1–6] This remarkable achievement fully highlights their great commercial potential. However, stability issues have emerged as a major obstacle, severely impeding their widespread application. The degradation of PSC stability stems from three fundamental sources: the intrinsic instability of perovskite materials themselves, interfacial charge recombination losses, and extrinsic environmental degradation pathways.[7] Among these, defects and mismatches at the interface can trigger ion migration, while the penetration of metal electrodes accelerates the degradation of perovskite materials—both of which are key factors undermining the stability of the solar cells.[8–10] Meanwhile, the interface between perovskites and the charge transport layer suffers from problems such as charge accumulation and energy loss.[11–14] Notably, the interface between the electron transport layer and the top electrode exerts a significant impact on the overall performance of the solar cells. To surmount these challenges, researchers have conducted extensive investigations in diverse fields, including material optimization, interface engineering, novel structural design, and packaging. Their endeavors focus on addressing the critical issues that hinder commercialization, aiming to develop more efficient and stable PSCs. Among numerous optimization strategies, interfacial buffer layers have proven particularly effective in simultaneously improving the photovoltaic performance and operational stability of PSCs.[15–18] By improving the energy level matching, reducing the accumulation of interfacial charge, blocking the erosion of external factors, and inhibiting ion migration, buffer layers can effectively retard material degradation, thereby boosting the efficiency and stability of PSCs.[19] Bathocuproine (BCP), as a commonly used buffer material, possesses numerous advantages and has been extensively applied in PSCs.[19–22] Firstly, BCP converts the Schottky contact between the electrode layer and the metal layer into an ohmic contact, which enhances the efficiency of charge

[a]College of Electrical Engineering & New Energy China Three Gorges University Yichang, Hubei 443002, P. R. China. E-mail: xiangpeng@ctgu.edu.cn

[b]Hubei Provincial Engineering Research Center for Solar Energy High-value Utilization and Green Conversion, College of Materials and Chemical Engineering, China Three Gorges University Yichang, Hubei 443002, P. R. China. E-mail: tanxin@ctgu.edu.cn

† Electronic supplementary information (ESI) available. See DOI: https://doi.org/10.1039/d5ta03658e

extraction and reduces interfacial recombination.[19,23,24] Secondly, BCP serves as an effective energy level modifier, optimizing interfacial band alignment across device layers to promote efficient charge carrier transport.[25] Thirdly, the BCP molecule can uniformly fill grain boundaries of perovskite, passivate the undercoordinated Pb^{2+} and I^- defects, and decrease carrier recombination.[25] Fourthly, the BCP layer can block the diffusion path of iodine ions in perovskite, prevent the penetration of metal electrodes, and decelerate the degradation of materials.[26] Nevertheless, BCP exhibits poor thermal stability. Zheng *et al.*[27] showed that BCP aggregates rapidly even at low temperatures (85 °C), resulting in significant deterioration of device performance. This aggregation increases the interface resistance, disrupts the charge transport process, and ultimately decreases the PCE of the PSCs. Meanwhile, the crystallization of BCP under thermal stress can alter the morphology of the film and increase the surface roughness, which further undermines the long-term stability of the device.[28] Zhu *et al.* engineered the electron transport system in planar PSCs by incorporating a YbO_x interlayer, fabricated through physical vapor deposition, between the ETL and metal electrode. This architecture demonstrated significantly enhanced device stability.[29] Huan Li *et al.* replaced BCP with a dense SnO_2 buffer layer at the cathode interface.[30] This interfacial modification substantially mitigated cathode-side charge accumulation while simultaneously suppressing Ag^+ and I^- ion migration, ultimately improving both the V_{OC} and thermal stability of the module-scale devices. Zheng *et al.* investigated an alternative device architecture by eliminating the BCP buffer layer while increasing the C_{60} thickness from 25 nm to 80 nm, aiming to simplify the interfacial structure while maintaining charge extraction efficiency. Although the device achieved good thermal stability, its efficiency remained low.[27] Nguyen *et al.* substituted the 2,9 positions of BCP with aromatic phenyl and *p*-toluene groups. This modification was highly effective in improving the flatness of the conjugated backbone and protecting the reactive nitrogen atom of the phenanthroline core, thus promoting charge transport and enhancing device stability. The modified BCP significantly enhanced charge transport, reduced recombination losses, and notably improved the structural stability of PSCs, thereby extending the device lifetime.[31] In summary, while various strategies have been explored as alternatives to BCP for improving device stability, there remains a paucity of research that directly addresses the thermal stability issue of BCP itself.

This work employs ethoxylated PEIE to enhance the overall stability of BCP-based devices. The pyridine nitrogen atom in BCP has lone pairs of electrons that can serve as hydrogen bond acceptors. These electrons form N–H···N and O–H···N hydrogen bonds with the hydrogen atoms from the –NH and –OH groups in PEIE. This interaction is anticipated to suppress the aggregation of BCP molecules under thermal stress, thereby improving the thermal stability of the solar cells. The incorporation of PEIE serves a dual function: it simultaneously resolves BCP's thermal instability while enhancing charge transport kinetics in perovskite photovoltaics, presenting a comprehensive strategy for high-performance stable PSCs.

2. Results and discussion

2.1 Interaction of PEIE with BCP

The structure of the PSCs in this paper is illustrated in Fig. 1a. The chemical structure and interaction between BCP and PEIE are depicted in Fig. 1b. We hypothesize that –NH and –OH groups in PEIE form N–H···N and –OH···N hydrogen bonding. To further validate this hypothesis, we employed Fourier

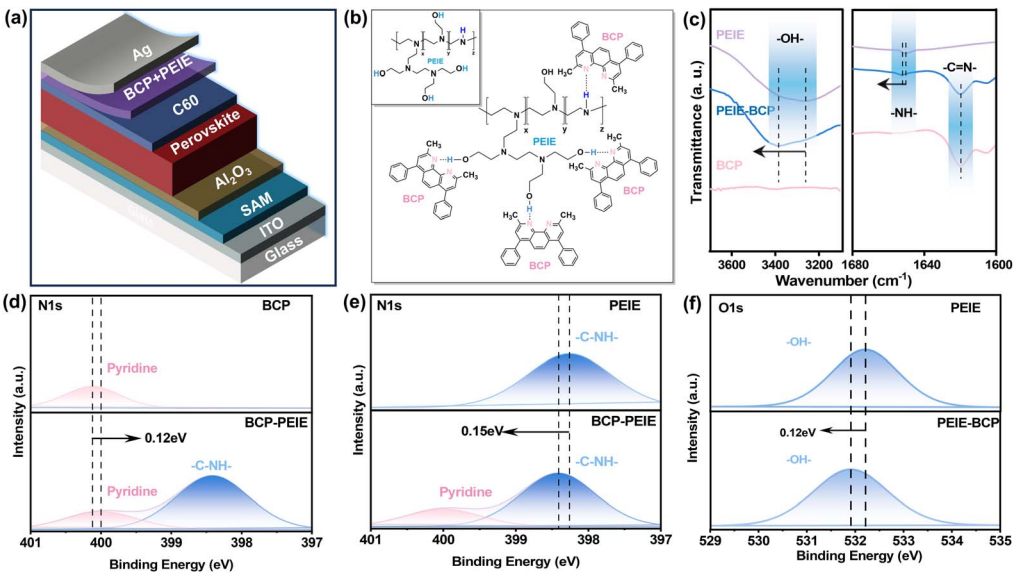

Fig. 1 (a) Schematic diagram of the PSC device structure. (b) Schematic diagram of the interaction between PEIE and BCP. (c) FTIR spectra of PEIE, BCP-PEIE and BCP. (d) N 1s XPS spectra of BCP and BCP-PEIE films. (e) N 1s XPS spectra of PEIE and BCP-PEIE films. (f) O 1s XPS spectra of PEIE and BCP-PEIE films.

transform infrared spectroscopy (FTIR) and X-ray photoelectron spectroscopy (XPS) to analyze the interaction between PEIE and BCP (Fig. S1†). As depicted in Fig. 1c, the FTIR vibration peaks of –OH and –NH in PEIE are redshifted from 3260.15 cm^{-1} and 1650.20 cm^{-1} to 3384.42 cm^{-1} and 1652.14 cm^{-1}, respectively. Meanwhile, the hydrogen bond acceptor C=N– exhibited a significant stretching vibration at 1619.68 cm^{-1}. As illustrated in Fig. 1e and f, due to hydrogen-bond formation, the binding energies of –NH (398.26 eV) and –OH (531.79 eV) in PEIE increased to 398.41 eV and 531.91 eV, respectively, with increments of 0.15 eV and 0.12 eV. This indicated that, as hydrogen bond donors, –NH and –OH redistributed electron cloud density with BCP. Meanwhile, as shown in Fig. 1d, the binding energy of pyridine N in BCP, originally 400.12 eV,[25] slightly decreases to 400.00 eV (a change of −0.12 eV), further confirming its role as a hydrogen bonding acceptor in hydrogen bond formation. XPS analysis further validates the occurrence of hydrogen bonding. The hydrogen bonding strengthens the π–π conjugation effect of BCP molecules.[32] The improved molecular arrangement enables tighter packing, resulting in a more densely crosslinked polymer network. Consequently, it effectively suppresses the aggregation of BCP molecules and influences the distribution of the electron cloud.[33]

The SEM image in Fig. 2a demonstrates the aggregation of BCP particles after heating at 85 °C for 10 hours. As the heating time extended, large aggregate grains were observed to appear on the BCP film. In contrast, the SEM images of BCP with addition of PEIE did not show significant aggregation (Fig. 2b). As depicted in Fig. S2,† the grain size distribution of BCP during heating was calculated. The average grain size increased from 18.72 μm to 43.41 μm as the heating time elapsed, which is consistent with the results presented in Fig. 2a. Fig. S3a† displays the AFM image of the BCP aggregation process. As the heating duration increased, the BCP film exhibited greater surface roughness and developed larger aggregated grains. However, for the AFM image of BCP with PEIE (Fig. S3b†), there

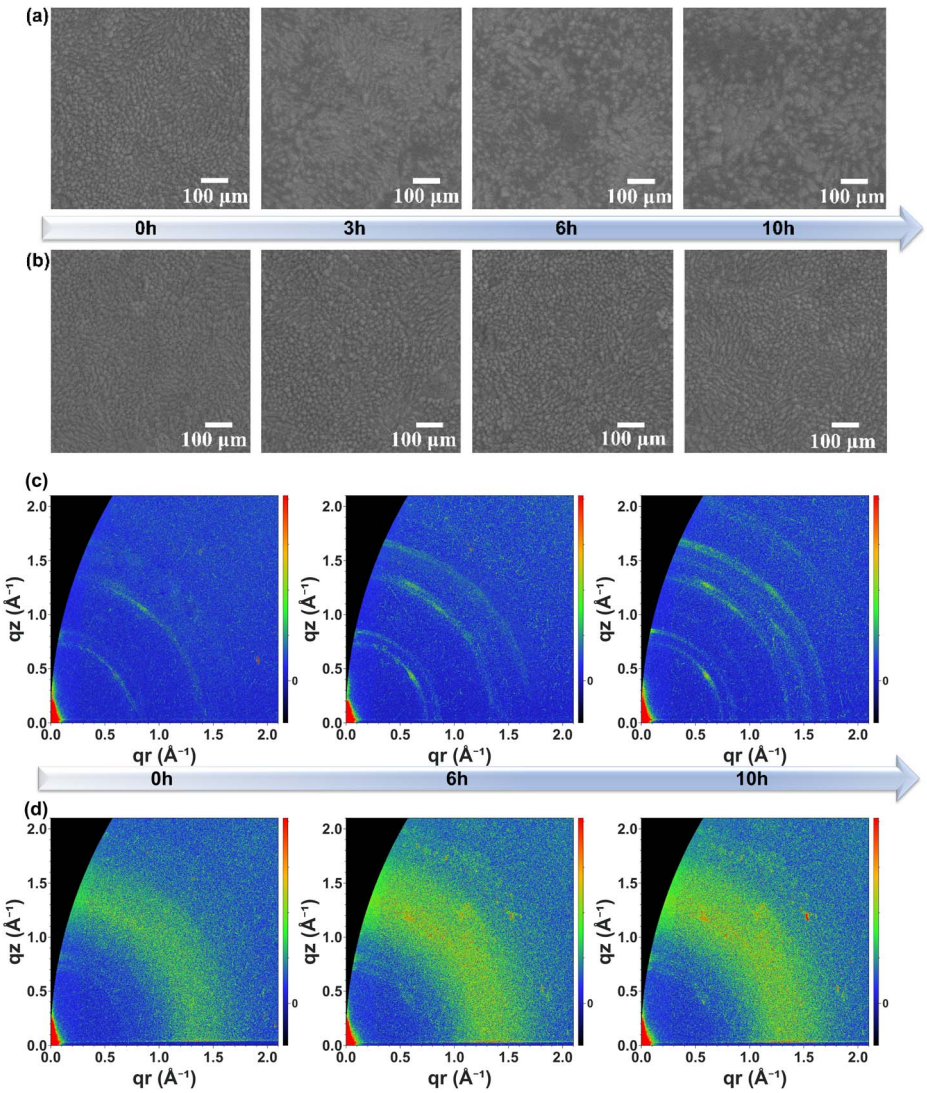

Fig. 2 (a) SEM images of ITO/BCP and (b) ITO/BCP-PEIE samples following thermal treatment at 85 °C for 10 h. GIWAXS images of the (c) BCP film and (d) BCP-PEIE film during heating at 85 °C for 0–10 hours.

was no significant change in roughness. To further investigate the thermal aggregation behavior of BCP films after heating at 85 °C for 10 hours, grazing-wide-angle X-ray small-angle scattering (GIWAXS) analysis was performed. As shown in Fig. 2c, with increasing heating time, the surface of the BCP film gradually became rougher, and the aggregation phenomenon intensified significantly. The GIWAXS pattern indicated that as the heating time increased, scattering signals in both the q_z and q_r directions changed, particularly in the vertical direction, where the Bragg peaks widened. The crystal orientation became more disordered, displaying features similar to Debye–Scherrer rings, suggesting that the BCP film underwent aggregation and disorder during heating.[34] In contrast, for the PEIE-modified BCP, as shown in Fig. 2d, despite being subjected to the same heating conditions, the surface remained relatively uniform. GIWAXS analysis revealed minimal changes in the scattering signals, and the Bragg peaks did not significantly broaden or blur, indicating that PEIE effectively suppressed thermal aggregation and enhanced the thermal stability of the film.

To determine whether the aggregation of BCP at 85 °C is a chemical polymerization or a physical process, Fourier transform infrared (FTIR) spectroscopy and differential scanning calorimetry (DSC) were performed on BCP films both before and after thermal treatment. As illustrated in Fig. 3a, the FTIR spectra of BCP films before and after heating at 85 °C exhibit no new characteristic peaks and significant peak shifts. This suggests that no new bonds form between BCP molecules at this temperature. DSC was utilized to examine the thermal properties of BCP under various conditions. As depicted in Fig. 3b, the DSC curve shows no significant endothermic or exothermic peaks in the temperature range from room temperature to 240 °C, indicating that no significant phase transitions or chemical reactions occur in the BCP. Collectively, the results of FTIR and DSC analyses indicate that the aggregation of BCP at 85 °C is primarily a physical process rather than a heat-induced chemical transition. In the PEIE-modified samples, the aggregation of BCP was significantly reduced, which indicates that the incorporation of PEIE effectively suppressed the heat-induced aggregation of BCP molecules. However, such aggregation had a detrimental impact on the device efficiency. As shown in Fig. 3c, after heating at 85 °C for 10 h, the V_{OC}, J_{SC}, FF and PCE of the control device decreased from 1.171 V, 25.38 mA cm^{-2}, 84.71, and 24.93% to 1.137 V, 20.78 mA cm^{-2}, 75.77, and 17.91%, respectively. On the one hand, the accumulation of BCP grains reduces the effective contact area between the buffer layer and the metal electrode, which in turn leads to a decrease in J_{SC}.[28] Simultaneously, this suboptimal contact increases the series resistance (R_s), reduces the recombination resistance (R_{re}), and consequently decreases both FF and V_{OC}.[28] In contrast, due to the suppression of BCP aggregation, the performance degradation of the modified device after heating is significantly mitigated (Fig. 3d).

The addition of PEIE not only suppresses the aggregation of BCP upon heating, but also enhances the crystallization of BCP. Fig. 3e and f are SEM images of the BCP layer and BCP-PEIE layer deposited on the perovskite/C_{60} film, respectively. SEM characterization confirms that the BCP layer modified with PEIE forms a uniform and pinhole-free dense coating on the C_{60} thin film. This characteristic is crucial for isolating the perovskite layer from the air. Conversely, the BCP layer deposited on a thin C_{60} film exhibits pinholes on its surface. These pinholes function as carrier recombination sites, inducing charge accumulation and conduction losses that degrade device performance. Concurrently, they provide pathways for water and oxygen infiltration to the perovskite layer, accelerating device instability. The water contact angle of the BCP-PEIE film (70.15°) is

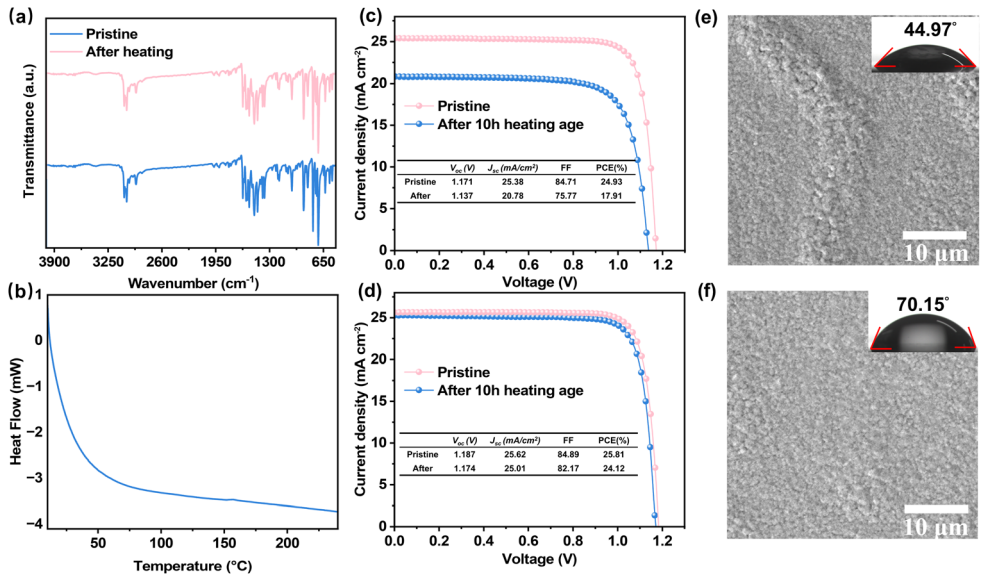

Fig. 3 (a) FTIR spectra of ITO/BCP before and after heating for 10 h. (b) DSC curves of BCP heated from room temperature to 240 °C. (c) Efficiency comparison of ITO/SAM/Al_2O_3/perovskite/C_{60}/BCP/Ag devices before and after heating at 85 °C for 10 hours. (d) Efficiency comparison of ITO/SAM/Al_2O_3/perovskite/C_{60}/BCP-PEIE/Ag structure devices before and after heating at 85 °C for 10 hours. SEM images and water contact angle of BCP films (e) and BCP-PEIE films (f) spin-coated on ITO/SAM/Al_2O_3/perovskite/C_{60}, respectively.

larger than that of the BCP film (44.97°). This difference can be attributed to the long carbon chain in the PEIE polymer, which further enhances the hydrophobicity of the BCP-PEIE composite.[35] To thoroughly characterize the morphological properties of both BCP and PEIE-modified BCP films, atomic force microscopy (AFM) was performed on samples deposited on C_{60} substrates. Fig. S4† shows the perovskite film morphology with a measured root mean square (RMS) roughness of 44.9 nm. When C_{60} is deposited on a perovskite film, the RMS roughness decreases to 29.8 nm. Depositing BCP on perovskite/C_{60} results in an RMS roughness of 46.8 nm. In contrast, depositing BCP-PEIE on perovskite/C_{60} yields a lower RMS roughness of 27.3 nm. A lower roughness value promotes better interface contact and charge transport.[36] Thus, the incorporation of PEIE not only improves the topography of the film and hydrophobicity but also enhances the overall performance of the device.

2.2 PEIE for PSC performance improvements

Fig. 4a shows the steady-state photoluminescence (PL) of PSCs with different transport layers spin-coated on top of the perovskite. As the number of layers increases, the PL peak intensity of the perovskite decreases significantly. When the perovskite layer is in contact with the ETL, a significant photoluminescence (PL) quenching phenomenon is expected theoretically. This occurs because the ETL efficiently extracts and transfers light-induced electrons before the carrier recombination takes place.[36] The observed enhancement in PL quenching efficiency for the C_{60}/BCP-PEIE ETL interface suggests more favorable energy alignment and reduced interfacial recombination losses compared to the conventional C_{60}/BCP ETL. This finding is consistent with the improved morphology of the BCP-PEIE layer (Fig. 3f). Moreover, time-resolved photoluminescence (TRPL) mapping reveals spatial variations in carrier lifetime (Fig. 4b and c). In Fig. 4b, the blue and green regions are distributed unevenly, with a noticeable "void" or low-lifetime area appearing near the center, which may indicate the presence of film defects such as porosity or surface inhomogeneity (Fig. 3e and S4c†). These defects generally introduce additional non-radiative recombination centers, which accelerate exciton recombination and thus reduce the photoluminescence (PL) lifetime in these regions. In contrast, the color distribution in Fig. 4c is significantly more uniform, with an overall shift towards green, yellow, and orange regions, indicating improved PL lifetime and enhanced spatial uniformity across the entire film (Fig. 3f and S4d†). This result aligns well with the expected improvements in film surface quality, such as reduced porosity and surface roughness. A smoother and denser film surface effectively minimizes defect states, thereby suppressing non-radiative recombination processes.[37]

To quantitatively characterize the trap density of states, two device architectures were fabricated: ITO/C60/BCP-PEIE/Ag and ITO/C60/BCP/Ag. The dark current–voltage (J–V) curves of their space charge-limiting currents (SCLC) at various voltages were measured, as depicted in Fig. 4d. The trap density of states (n_{trap}) was calculated using the following equation (eqn (1)):[38]

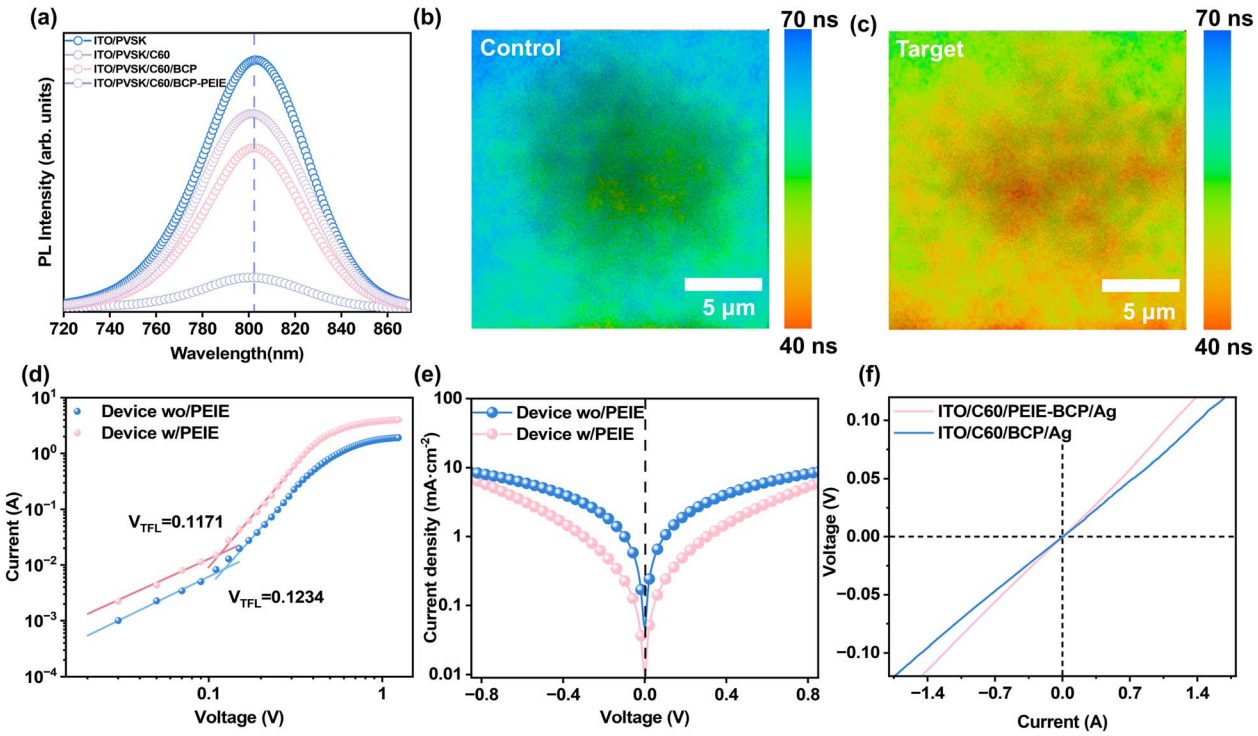

Fig. 4 (a) PL spectra of perovskite (PVSK), PVSK/C60, PVSK/C_{60}/BCP and PVSK/C_{60}/BCP-PEIE. (b) TRPL mapping image of BCP/C60/perovskite. (c) TRPL mapping image of BCP-PEIE/C60/perovskite. (d) Space charge limited current (SCLC) plots based on BCP and BCP-PEIE devices, respectively. (e) Dark J–V curves based on BCP and BCP-PEIE devices, respectively. (f) V–I curves of ITO/C_{60}/BCP/Ag and ITO/C_{60}/BCP-PEIE/Ag structural devices.

$$n_{trap} = \frac{2\varepsilon\varepsilon_0 V_{TFL}}{eL^2} \quad (1)$$

where V_{TFL} denotes the trap – filled limiting voltage, ε_0 (8.854×10^{-12} F m^{-1}) represents the vacuum permittivity, ε (25) is the relative permittivity of the semiconductor material, e (1.602×10^{-19} C) is the elemental charge, and L (450 nm) is the thickness of the measured film. The incorporation of PEIE leads to a noticeable reduction in the V_{TFL} of the device, decreasing from 0.1234 V to 0.1171 V. Compared to pristine BCP films, the trap density (n_{trap}) in BCP-PEIE composite films decreases from 6.04×10^{15} cm^{-3} to 5.73×10^{15} cm^{-3}. This reduction in trap density effectively suppresses charge accumulation at the interface. Such an effect is attributed to the enhanced structural stability of the BCP film upon the introduction of PEIE. As illustrated in Fig. 4e, the dark current density of the device incorporating the BCP-PEIE interlayer is markedly reduced within the voltage range of −0.8 V to 0.8 V, which contributes to an enhancement in the open-circuit voltage (V_{OC}). As illustrated in Fig. 4f, this stable crystal structure endows the C_{60}/BCP-PEIE electron transport layer (ETL) with superior properties compared to the C_{60}/BCP ETL, thereby facilitating efficient charge transport within the device. To further explore the charge recombination behavior, we analyzed the relationship between V_{OC} and light intensity, along with transient photovoltage decay. The slope obtained from the V_{OC} *versus* light intensity curve reflects the extent of trap-assisted recombination and corresponds to the ideality factor.[39] As shown in Fig. S5,† the devices with the C_{60}/BCP-PEIE ETL exhibit a relatively small slope of $1.20K_BT/q$, whereas the devices with the C_{60}/BCP ETL exhibit a larger slope of $1.38K_BT/q$. This indicates that the C_{60}/BCP-PEIE ETL reduces the Shockley–Read–Hall recombination. Fig. S6† shows the UV-vis absorption spectra of the films. The absorption intensities of the perovskite/BCP and perovskite/BCP–PEIE films are nearly identical. The introduction of PEIE does not affect the original thickness of the BCP layer; thus, its influence on the optical absorption of the perovskite layer can be considered negligible.[40]

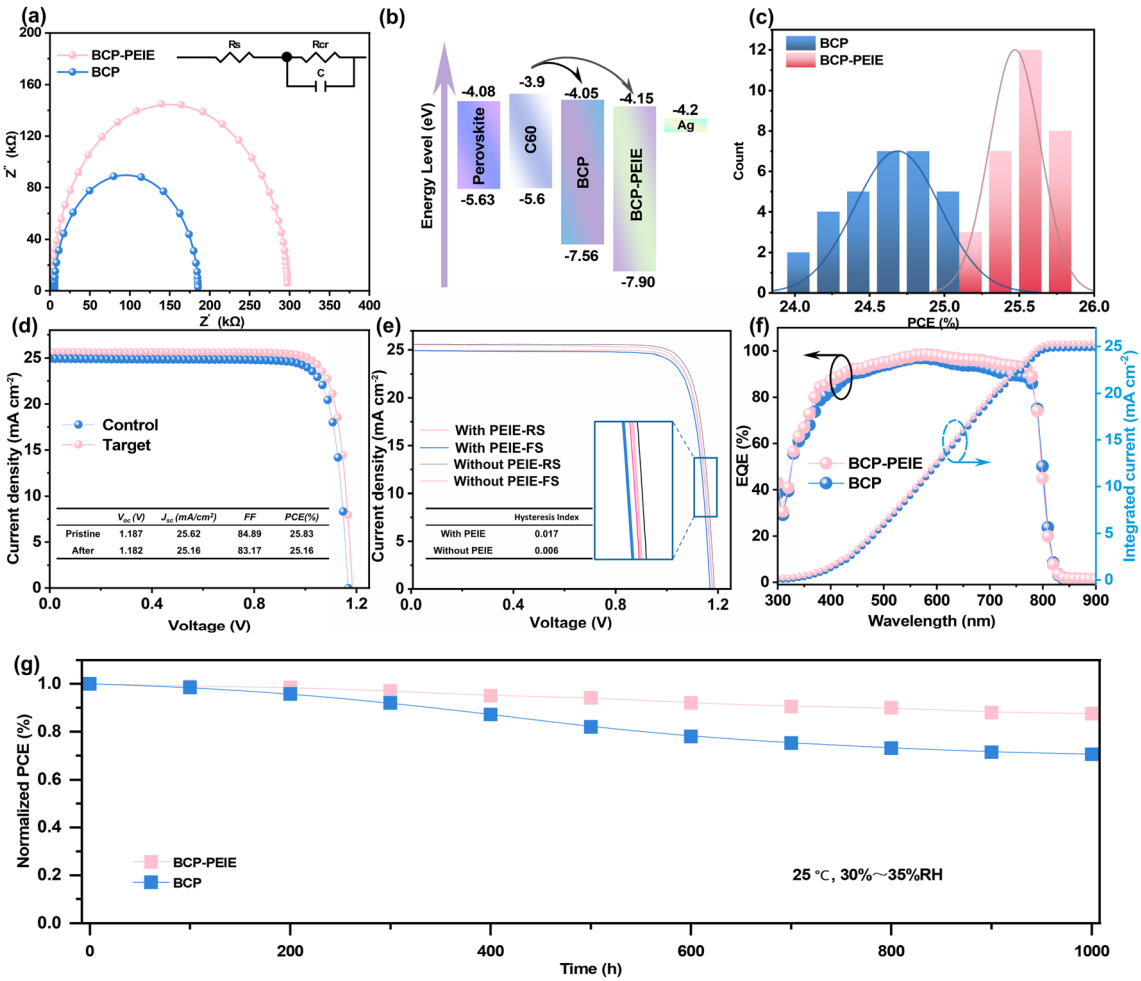

Fig. 5 (a) Electrical impedance response of PSC devices with C_{60}/BCP and C_{60}/BCP-PEIE as the ETL, along with the equivalent circuit model used for fitting the corresponding measurement data. (b) Energy level alignment diagram. (c) PCE distribution of PSCs with the C_{60}/BCP ETL and C_{60}/BCP-PEIE ETL from 30 device statistics, respectively. (d) J–V curves of optimal BCP and BCP-PEIE PSCs. (e) J–V curves of BCP and BCP-PEIE PSCs under forward and reverse scans. (f) EQE spectra of PSCs based on BCP and BCP-PEIE. (g) Moisture stability at 30–35% relative humidity (RH) in air at 25 °C.

Fig. 5a displays the Nyquist plot and the corresponding equivalent circuit for the devices based on C_{60}/BCP and C_{60}/BCP-PEIE. The equivalent circuit comprises a series resistor (R_s), a recombination resistor (R_{re}), and a capacitor. The values of these resistors are summarized in Table S2.† Compared to the control devices, the BCP-PEIE-modified devices exhibit lower R_s and higher R_{re} values. This suggests improved charge transport efficiency and suppressed non-radiative recombination losses.[41]

In this section, the influence of PEIE on the improvement of BCP energy levels is investigated. The energy level alignment presented in this study was derived from ultraviolet photoelectron spectroscopy (UPS) and UV-vis absorption measurements, as shown in Fig. S7† and 5b. According to Fig. S7f and S7g,† the $E_{cut\text{-}off}$ energies of BCP and BCP-PEIE are 17.00 eV and 17.11 eV, respectively. The Fermi level can be calculated using the formula $E_F = E_{cut\text{-}off} - 21.22$. Thus, the Fermi levels of BCP and BCP-PEIE are −4.22 eV and −4.11 eV, respectively. The valence band maximum (V_{BM}) is determined using the equation $E_{VB} = E_F - E_{F,edge}$. The $E_{F,edge}$ of BCP and BCP-PEIE was 3.20 eV and 3.79 eV, respectively, and the corresponding E_{VB} for BCP and BCP-PEIE was −7.42 eV and −7.32 eV, respectively. As shown in Fig. S7d and e,† the band gaps (E_g) of BCP and BCP-PEIE were calculated to be 3.51 eV and 3.75 eV. Using the formula $E_{CB} = E_{VB} + E_g$, the conduction band minimum (C_{BM}) of the pristine BCP and BCP-PEIE was −3.91 eV and −4.23 eV, respectively. Clearly, this cascaded energy level structure facilitates efficient electron extraction from the perovskite to the electron transport layer (ETL), effectively reducing interfacial charge buildup and recombination processes.[42] Moreover, BCP-PEIE has a deeper valence band maximum than BCP, which enables more effective blocking of holes and suppression of carrier recombination.[43–45]

To evaluate the impact of PEIE on the performance and stability of the device, we fabricated planar PSCs with ITO/SAM/Al_2O_3/perovskite/C_{60}/BCP-PEIE/Ag structures. Here, BCP solutions containing different concentrations of PEIE ranging from 0 to 0.9 mg mL^{-1} were prepared to determine the optimal concentration of PEIE for fabricating high-performance devices. The corresponding device performance is summarized in Table S1 (corresponding efficiency graph can be seen in Fig. S8).† To assess the repeatability of device performance, we counted the power conversion efficiencies (PCEs) of multiple devices and plotted a histogram of the efficiency distribution (Fig. 5c). The results indicate that the PEIE modified devices not only exhibit higher average efficiency but also have more concentrated efficiency distributions and smaller standard deviations. This suggests that the modification strategy has good reproducibility. From the statistical results, it is evident that the PCE of all BCP-PEIE devices is improved compared to that of BCP devices. This enhancement is attributed to the concurrent improvements in open-circuit voltage V_{OC}, J_{SC}, and FF. When the PEIE concentration was 0.6 mg mL^{-1}, the champion device had a V_{OC} of 1.187 V, a J_{SC} of 25.62 mA cm^{-2}, an FF of 84.89%, and a PCE of 25.81%, as shown in Fig. 5d. These performance metrics surpass those of the control device, which exhibited a V_{OC} of 1.179 V, a J_{SC} of 25.01 mA cm^{-2}, an FF of 84.71%, and a PCE of 24.98%. The photovoltaic performance of devices with different PEIE concentrations was systematically analyzed. The statistical results of 20 devices for each condition are summarized in Fig. S9.† Moderate PEIE concentrations (0.3 mg mL^{-1} and 0.6 mg mL^{-1}) significantly enhance J_{SC}, V_{OC}, FF, and PCE compared to unmodified BCP devices, confirming the positive interfacial passivation effect. However, excessive PEIE (0.9 mg mL^{-1}) leads to performance degradation, which is likely due to the fact that an excessive amount of PEIE hinders efficient electron transport and extraction. These results demonstrate the existence of an optimal PEIE concentration window for efficient device operation.[46] As shown in Fig. S10a,† in order to investigate the effect of different PEIE concentrations on device performance, we measured the electrical impedance response of devices fabricated from BCP solutions containing various PEIE concentrations. It is evident that the devices incorporating PEIE exhibit lower R_s and higher R_{re} compared to the control devices, confirming the enhanced charge transport and suppressed non-radiative recombination, which are responsible for the improvement in FF. However, with the further increase in PEIE concentration, R_s gradually increases while R_{re} decreases, which leads to a decline in both J_{SC} and FF. These results are consistent with the statistical data shown in Fig. S9a.†[46] Fig. S10b† demonstrates that PEIE enhances the electron transport capability of the device. However, as the concentration increases, the electron transport capability further decreases, which corresponds well with the results shown in Fig. S9.†

It is important to highlight that despite the incorporation of PEIE into the BCP layer, there is no notable change in the device's hysteresis behavior, as shown in Fig. 5e (the corresponding efficiency data are presented in Table S3.†). The hysteresis index (HI) was calculated using the formula:

$$HI = \frac{PCE_{rev} - PCE_{fwd}}{PCE_{rev}} \quad (2)$$

where PCE_{rev} and PCE_{fwd} refer to the PCE at the same voltage point during reverse and forward scans, respectively. The calculated hysteresis indices are 0.006 for the control device and 0.017 for the PEIE-modified device, indicating that the introduction of PEIE has a negligible impact on device hysteresis.

This indicates that PEIE does not have a negative impact on interfacial charge transport. Moreover, this result further implies that the improvement in stability in PEIE-modified devices is not due to a change in the hysteresis effect, but may be related to the enhanced stability of the BCP morphology and the suppression of aggregation. To gain deeper insight into the photoelectric conversion performance, external quantum efficiency (EQE) spectra were measured, as shown in Fig. 5f. The data reveal that the EQE of the PEIE-modified devices is enhanced across the entire spectral range, with a notable improvement in the 400–700 nm range. The integrated current density increased from 24.81 mA cm^{-2} to 25.38 mA cm^{-2}, an increase of approximately 0.57 mA cm^{-2}. This indicates that the collection capacity of photogenerated carriers is enhanced, which is consistent with the PL test results.

Since device stability is as crucial as efficiency,[47] this section assesses the impact of PEIE-modified BCP on the device stability. The maximum power point of the champion device was continuously tracked under AM 1.5 illumination. To thoroughly assess the device's long-term stability, an unpackaged device underwent a standard light stability test in a nitrogen (N_2) atmosphere. As depicted in Fig. S11,† the device with a BCP electron transport layer without PEIE could only retain 84.29% of its initial efficiency under continuous illumination, whereas the PEIE modified BCP device could still retain up to 96.08% of its initial efficiency. This result clearly demonstrates that PEIE modification significantly enhances the device stability. Fig. S12† presents the time-dependent water contact angle evolution of the unmodified BCP surface (Fig. S12a–c†) and the PEIE-modified BCP surface (Fig. S12d–f†) under 70% RH. For the unmodified BCP, the initial contact angle is 42°, which decreases rapidly to 40° within 20 seconds and further drops to 19° after 50 seconds, indicating poor hydrophobicity and significant moisture interaction. In contrast, the PEIE-modified BCP exhibits an initial contact angle of 61°, which remains relatively high (57° at 20 seconds and 53° at 50 seconds) compared to the unmodified sample. This suggests that PEIE significantly enhances the hydrophobicity of the BCP surface and delays water penetration under high humidity conditions. Fig. 5g demonstrates the moisture stability of PSCs under ambient conditions (relative humidity: 30–35%; temperature: 25 °C). After 1000 hours of storage, the target device still retained 87.5% of its initial efficiency.

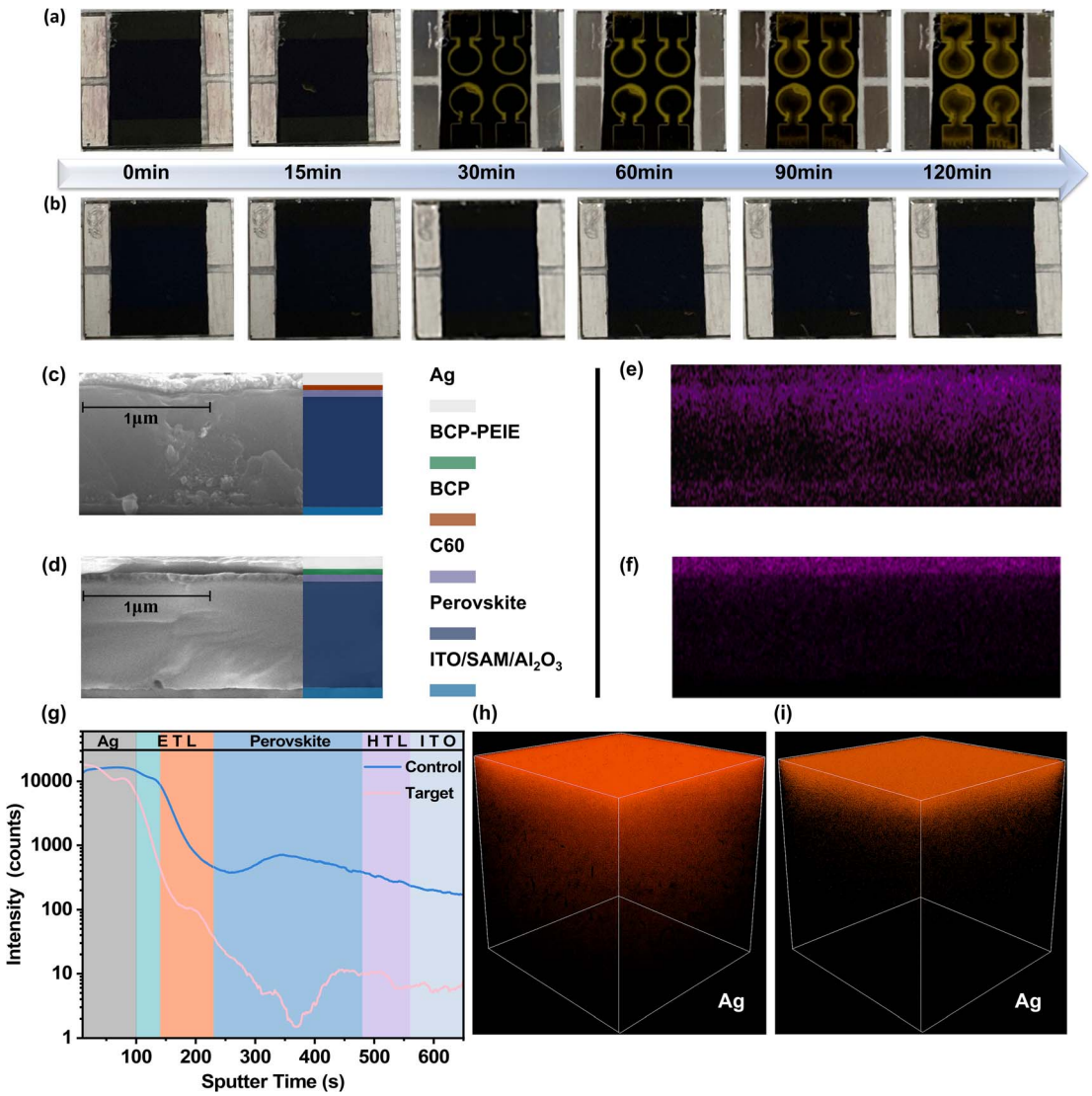

Fig. 6 (a) Images of ITO/SAM/Al_2O_3/perovskite/C_{60}/BCP/Ag and (b) ITO/SAM/Al_2O_3/perovskite/C_{60}/BCP-PEIE/Ag structure devices at different time intervals during heating to 200 °C for 120 minutes. Cross-sectional SEM image of the devices with BCP (c) and BCP-PEIE (d) after heating at 200 °C for 120 minutes. (e) Corresponding EDS images of the devices with the BCP layer after heating. (f) Corresponding EDS images of devices with the BCP-PEIE layer after heating. (g) ToF-SIMS depth profiles of the aged PSC device. (h) and (i) Reconstructed 3D elemental distribution maps of Ag ions for devices with BCP and BCP-PEIE layers, respectively, obtained from depth profiling analysis.

2.3 PEIE improves the thermal stability of the device

To further explore the impact of BCP aggregation on thermal stability, Fig. 6a illustrates that when a PEIE-free device is heated at 200 °C for 120 min. Ag ions gradually permeate downward. This phenomenon occurs because the aggregation of BCP forms large grains, creating significant voids in the BCP film that allow Ag to permeate under high-temperature conditions. In contrast, since PEIE suppresses the aggregation of BCP, it effectively hinders the diffusion of Ag (Fig. 6b). As shown in Fig. S13,† the front surface of the device exhibits no noticeable changes. Devices incorporating BCP-PEIE show no obvious Ag ion permeation within the 0–120 minute timeframe. As shown in Fig. 6d, a significant amount of aggregation appears at the cross-section of the device without PEIE, which may be the result of some of the permeated Ag ions reacting with I^- to form AgI.[48,49] The presence of PEIE forms a physical barrier film, resulting in almost no Ag detection at the interface. This difference is clearly demonstrated by the corresponding energy-dispersive X-ray spectroscopy (EDS) results (Fig. 6e–f). The distribution of Ag in the perovskite layer of the devices containing PEIE is significantly lower than that in the devices without PEIE.

To further investigate the barrier effect of BCP-PEIE on metal ion migration, time-of-flight secondary ion mass spectrometry (TOF-SIMS) depth profiling and 3D elemental mapping were performed on aged devices with BCP and BCP-PEIE layers. As shown in Fig. 6g, the Ag depth profile reveals significant silver diffusion into the device bulk for the control sample using BCP as the ETL. Even after extended sputtering, strong Ag signals are still detected in the perovskite and HTL regions, indicating severe Ag migration during aging, which could be detrimental to device stability. In contrast, for the modified device with BCP-PEIE, the Ag signal intensity sharply decreases upon entering the ETL region, with only a small amount of Ag detected in the perovskite layer, demonstrating that the introduction of PEIE effectively suppresses Ag diffusion. The corresponding 3D reconstructed Ag distributions, shown in Fig. 6h and i, further support this conclusion. In the control device (Fig. 6h), Ag particles are not only concentrated at the top electrode but also exhibit obvious downward penetration into the device interior. However, in the BCP-PEIE modified device (Fig. 6i), Ag remains predominantly confined to the electrode interface, with minimal downward diffusion observed.

These results collectively confirm that the incorporation of PEIE significantly enhances the interfacial barrier properties of BCP, effectively suppressing Ag migration under thermal aging conditions and thereby contributing to the improved operational stability of the device.

3. Conclusion

In this study, we successfully addressed the high temperature aggregation issue of BCP by introducing PEIE. Experimental results revealed that the –NH and –OH groups in PEIE, acting as hydrogen bond donors, form hydrogen bonds with the pyridine nitrogen atoms in BCP. This interaction enhances π–π stacking between BCP molecules and suppresses molecular aggregation. PEIE optimizes the energy level alignment of BCP, facilitating more efficient carrier transport. Moreover, the incorporation of PEIE results in a denser and more uniform BCP film. The contact angle on the surface acts as a protective barrier, effectively preventing moisture from infiltrating the perovskite absorber layer from the air. During the thermal stability test, the BCP-PEIE film inhibits the infiltration of Ag ions, thereby improving the thermal stability of the device. As a result, the device incorporating PEIE achieved a PCE of 25.81% and maintained a PCE retention rate of over 86.5% after 1000 hours of operation at 30% relative humidity. In summary, this study provides a simple strategy to overcome the thermal stability challenges of BCP buffer materials in PSCs. This approach is expected to accelerate the development of high-efficiency and stable PSCs, laying a stronger foundation for their commercialization.

4. Experimental section

4.1 Device preparation

The ITO conductive glass was ultrasonically cleaned in deionized water, absolute ethanol, and isopropanol for 15 minutes. It was then dried using high-pressure nitrogen and subjected to ultraviolet ozone treatment for 30 minutes. A self-assembled monolayer (SAM) solution (0.5 mg mL^{-1}) of 4-PADCB was spin-coated onto the ITO substrates at 3000 rpm with an acceleration of 1000 rpm s^{-1} for 30 seconds. The coated substrates were annealed on a hot stage at 100 °C for 10 minutes under ambient air conditions. The Al_2O_3 (0.5 mg mL^{-1}) reagent was diluted with deionized water in a 1 : 5 ratio. The prepared Al_2O_3 solution was then spin-coated onto the SAM layer at 5000 rpm with an acceleration of 3000 rpm s^{-1} for 20 seconds. For the perovskite layer, a two-step spin-coating process was employed. In the first step, the precursor solution was spin-coated onto the Al_2O_3 layer at 2000 rpm with an acceleration of 2000 rpm s^{-1} for 25 seconds. In the second step, the speed was increased to 5000 rpm with an acceleration of 2000 rpm s^{-1} for 23 seconds. At the 13th second of the second stage, 120 μL of chlorobenzene was dropwise added onto the spinning substrate. Finally, the samples were annealed at 110 °C for 20 minutes. After that, a 250-nm-thick C_{60} ETL was deposited. A 0.5 mg per mL BCP solution was prepared using isopropyl alcohol. Different concentrations of PEIE were added to this solution, and then the resulting BCP solutions (with or without PEIE) were spin-coated onto the C_{60} layer at 6000 rpm, with an acceleration of 3000 rpm s^{-1} for 30 seconds.

4.2 Materials

ITO-coated glass substrates were purchased from Guangzhou Sunyoung Technology Co., Ltd. SAM (4PADCB) was obtained from TCI. *N*,*N*-Dimethylformamide (DMF, ≥99.99%) was purchased from Alfa Aesar. Chlorobenzene (CB, ≥99.99%) and dimethyl sulfoxide (DMSO, ≥99.99%) were purchased from Acros Organics. Ethanol (≥99%) was purchased from Aladdin. Aluminum oxide (Al_2O_3, ≥99.8%) was obtained from Sigma-Aldrich. C_{60} was purchased from Shanghai Weizhu Chemical

Technology Co., Ltd. Rubidium thiocyanate (RbSCN, ≥99.5%) was purchased from Suzhou Liwei New Material Technology Co., Ltd. 2-Fluoroethylammonium chloride (FEACl, 98%) was purchased from Alfa Aesar. Cesium iodide (CsI, 99.5%), lead(II) chloride ($PbCl_2$, 99.99%), methylammonium iodide (MAI, 99.99%), formamidinium iodide (FAI, 99.5%), lead(II) iodide (PbI_2, 99.99%), and bathocuproine (BCP, 99.5%) were purchased from Liaoning Youxuan New Energy Technology Co., Ltd. Polyethylenimine ethoxylated (PEIE, 37 wt% in H_2O) was purchased from Aldrich. Unless otherwise specified, all materials were used as received without further purification.

The perovskite precursor solution, with a nominal composition of $FA_{0.84}MA_{0.01}Cs_{0.04}Rb_{0.01}Pb(I_{0.89}Br_{0.11})_3$, was prepared by dissolving the corresponding salts in a mixed solvent of DMF and DMSO at a volume ratio of 4 : 1.

4.3 Characterization

A solar simulator with xenon lamps (Oriel 94023 A, Newport, USA) was used to calibrate the light intensity. Standard silicon solar cells were employed to generate AM 1.5 G radiation (100 mW cm^{-2}) in air. The current density–voltage (*J–V*) characteristics were measured using a source meter (Keithley 2400). The devices were tested without preprocessing, with voltage sweeps ranging from 1.35 V to 0.15 V (reverse sweep) and 0.15 V to 1.35 V (forward sweep), a step size of 10 mV, and a sweep rate of 100 mV s^{-1}. Scanning electron microscopy (SEM) images and energy dispersive spectroscopy (EDS) spot analysis data were obtained using a Zeiss Sigma 500. EDS mapping was performed with an FEI Helios 450S, and atomic force microscopy (AFM) measurements were conducted on a Bruker Dimension Fast Scan (USA). The water contact angle was measured with an optical video contact angle meter (VCA Optima XE, AST) at ambient temperature. Fourier-transform infrared (FTIR) spectra were recorded using a Thermo Fisher IS50 (USA). Steady-state photoluminescence (PL) spectra and transient PL decay (TRPL mapping) were measured using a PL spectrometer (HITACHI F 4700, Japan). Incident photoelectron conversion efficiency (IPCE) was measured using an IPCE system (QE-R, Enli Technology Co., Ltd). X-ray photoelectron spectroscopy (XPS) was conducted using a Thermo Fisher ESCAlab 250Xi, and ultraviolet photoelectron spectroscopy (UPS) data were collected using the same spectrometer with a 21.22 eV monochromatic He Iα source. Transmission spectra between 300 and 900 nm were recorded with a UV-2550 UV-Vis-NIR spectrophotometer (Shimadzu, Japan). The GIWAXS measurements were performed at SPring-8 BL46XU.

Data availability

The data that support the findings of this study are available in the ESI† of this article.

Author contributions

H. X. conceived the study, conducted the experiments, and wrote the manuscript. B. L. contributed to the initial research planning and experimental setup. H. X., P. L and K. Z. fabricated the devices and performed the characterization. P. X. and X. T. supervised the project. All authors participated in data analysis and discussion.

Conflicts of interest

The authors declare no conflict of interest.

Acknowledgements

This work was supported by the National Natural Science Foundation of China (Grant No. 52007104) and the 111 Project (D20015). The authors thank the Analytical and Testing Center of Huazhong University of Science and Technology, as well as the Center for Nanoscale Characterization & Devices (CNCD) at Wuhan National Laboratory for Optoelectronics, for their support in various characterization studies and measurements.

References

1 H. Chen, S. Teale, B. Chen, Y. Hou, L. Grater, T. Zhu, K. Bertens, S. M. Park, H. R. Atapattu, Y. Gao, M. Wei, A. K. Johnston, Q. Zhou, K. Xu, D. Yu, C. Han, T. Cui, E. H. Jung, C. Zhou, W. Zhou, A. H. Proppe, S. Hoogland, F. Laquai, T. Filleter, K. R. Graham, Z. Ning and E. H. Sargent, *Nat. Photonics*, 2022, **16**, 352–358.

2 Q. Jiang, J. Tong, Y. Xian, R. A. Kerner, S. P. Dunfield, C. Xiao, R. A. Scheidt, D. Kuciauskas, X. Wang, M. P. Hautzinger, R. Tirawat, M. C. Beard, D. P. Fenning, J. J. Berry, B. W. Larson, Y. Yan and K. Zhu, *Nature*, 2022, **611**, 278–283.

3 S. Liu, J. Li, W. Xiao, R. Chen, Z. Sun, Y. Zhang, X. Lei, S. Hu, M. Kober-Czerny, J. Wang, F. Ren, Q. Zhou, H. Raza, Y. Gao, Y. Ji, S. Li, H. Li, L. Qiu, W. Huang, Y. Zhao, B. Xu, Z. Liu, H. J. Snaith, N.-G. Park and W. Chen, *Nature*, 2024, **632**, 536–542.

4 W. Peng, K. Mao, F. Cai, H. Meng, Z. Zhu, T. Li, S. Yuan, Z. Xu, X. Feng, J. Xu, M. D. McGehee and J. Xu, *Science*, 2023, **379**, 683–690.

5 Q. Tan, Z. Li, G. Luo, X. Zhang, B. Che, G. Chen, H. Gao, D. He, G. Ma, J. Wang, J. Xiu, H. Yi, T. Chen and Z. He, *Nature*, 2023, **620**, 545–551.

6 M. A. Green, E. D. Dunlop, M. Yoshita, N. Kopidakis, K. Bothe, G. Siefer, D. Hinken, M. Rauer, J. Hohl-Ebinger and X. Hao, *Prog. Photovoltaics*, 2024, **32**, 425–441.

7 H. Zhu, S. Teale, M. N. Lintangpradipto, S. Mahesh, B. Chen, M. D. McGehee, E. H. Sargent and O. M. Bakr, *Nat. Rev. Mater.*, 2023, **8**, 569–586.

8 E. J. Juarez-Perez, L. K. Ono, M. Maeda, Y. Jiang, Z. Hawash and Y. Qi, *J. Mater. Chem. A*, 2018, **6**, 9604–9612.

9 M. Saliba, T. Matsui, J.-Y. Seo, K. Domanski, J.-P. Correa-Baena, M. K. Nazeeruddin, S. M. Zakeeruddin, W. Tress, A. Abate, A. Hagfeldt and M. Gratzel, *Energy Environ. Sci.*, 2016, **9**, 1989–1997.

10 X. Zhang, G. Li, G. Chen, D. Wu, X. Zhou and Y. Wu, *Coord. Chem. Rev.*, 2020, **418**, 213376.

11 K. Chen, W. Jin, Y. Zhang, T. Yang, P. Reiss, Q. Zhong, U. Bach, Q. Li, Y. Wang, H. Zhang, Q. Bao and Y. Liu, *J. Am. Chem. Soc.*, 2020, **142**, 3775–3783.
12 T. Chen, T. Shi, X. Li, J. Zheng, W. Fan, B. Ni, Y. Wang, J. Dai and Z. Xiao, *Sol. RRL*, 2018, **2**, 00167.
13 T. Leijtens, G. E. Eperon, S. Pathak, A. Abate, M. M. Lee and H. J. Snaith, *Nat. Commun.*, 2013, **4**, 2885.
14 Z. Xie, B. Zhang, Y. Ge, Y. Zhu, G. Nie, Y. Song, C.-K. Lim, H. Zhang and P. N. Prasad, *Chem. Rev.*, 2022, **122**, 1127–1207.
15 X. Liu, H. Yu, L. Yan, Q. Dong, Q. Wan, Y. Zhou, B. Song and Y. Li, *ACS Appl. Mater. Interfaces*, 2015, **7**, 6230–6237.
16 L. Chen, G. Wang, L. Niu, Y. Yao, Y. Guan, Y. Cui and Q. Song, *RSC Adv.*, 2018, **8**, 15961–15966.
17 Z. Zhu, Y. Bai, X. Liu, C.-C. Chueh, S. Yang and A. K. Y. Jen, *Adv. Mater.*, 2016, **28**, 6478–6484.
18 J. Seo, S. Park, Y. C. Kim, N. J. Jeon, J. H. Noh, S. C. Yoon and S. I. Seok, *Energy Environ. Sci.*, 2014, **7**, 2642–2646.
19 N. Shibayama, H. Kanda, T. W. Kim, H. Segawa and S. Ito, *APL Mater.*, 2019, **7**, 031117.
20 S. Asgary, H. M. Moghaddam, A. Bahari and R. Mohammadpour, *Sol. Energy*, 2021, **213**, 383–391.
21 J. P. Chen, T. W. Colburn, J. Risner-Jamtgaard, A. Vailionis, A. Barnum, M. Golding, A. Carbone, A. C. Flick and R. H. Dauskardt, *Matter*, 2025, **8**, 101990.
22 Z. Ying, X. Yang, J. Zheng, Y. Zhu, J. Xiu, W. Chen, C. Shou, J. Sheng, Y. Zeng, B. Yan, H. Pan, J. Ye and Z. He, *J. Mater. Chem. A*, 2021, **9**, 12009–12018.
23 W. Li, G. Wang, Y. Long, L. Xiao, Z. Zhong, X. Li, H. Xu, H. Yan and Q. Song, *ACS Appl. Mater. Interfaces*, 2024, **16**, 63019–63025.
24 Y. Liu, B. Long, R. Chen, S. Huang, W. Ou-Yang and X. Chen, *ACS Appl. Energy Mater.*, 2021, **4**, 3812–3821.
25 R. Chen, B. Long, S. Wang, Y. Liu, J. Bai, S. Huang, H. Li and X. Chen, *ACS Appl. Mater. Interfaces*, 2021, **13**, 24747–24755.
26 Y. Wang, J. Zhang, Y. Wu, Z. Yi, F. Chi, H. Wang, W. Li, Y. Zhang, X. Zhang and L. Liu, *Semicond. Sci. Technol.*, 2019, **34**, 1361–6641.
27 X. Zheng, T. Jiang, L. Bai, X. Chen, Z. Chen, X. Xu, D. Song, X. Xu, B. Li and Y. Yang, *RSC Adv.*, 2020, **10**, 18400–18406.
28 C.-C. Lee, W.-C. Su, J.-C. Huang, C.-F. Lin and S.-W. Liu, *J. Photonics Energy*, 2011, **1**, 011108.
29 P. Chen, Y. Xiao, J. Hu, S. Li, D. Luo, R. Su, P. Caprioglio, P. Kaienburg, X. Jia, N. Chen, J. Wu, Y. Sui, P. Tang, H. Yan, T. Huang, M. Yu, Q. Li, L. Zhao, C.-H. Hou, Y.-W. You, J.-J. Shyue, D. Wang, X. Li, Q. Zhao, Q. Gong, Z.-H. Lu, H. J. Snaith and R. Zhu, *Nature*, 2024, **625**, 516–522.
30 H. Li, G. Xie, J. Fang, X. Wang, S. Li, D. Lin, D. Wang, N. Huang, H. Peng and L. Qiu, *Nano Energy*, 2024, **124**, 109507.
31 T.-D. Nguyen, D. Yeo, R. K. Chitumalla, S.-J. Kim, G.-H. Jeong, D.-G. Kwun, J. Jang, I. H. Jung and J.-Y. Seo, *Adv. Energy Mater.*, 2025, **15**, 03633.
32 U. Ahmed, D. Sundholm and M. P. Johansson, *Phys. Chem. Chem. Phys.*, 2024, **26**, 27431–27438.
33 Y. Wu, S. Chen, J. Wu, F. Liu, C. Chen, B. Ding, X. Zhou and H. Deng, *Sci. Adv.*, 2024, **10**, 48.
34 P. Müller-Buschbaum, *Synchrotron Radiation in Materials Science: Light Sources, Techniques, and Applications*, 2018, vol. 1, p. 134.
35 C. Verma, K. Y. Rhee and M. A. Quraishi, *Adv. Colloid Interface Sci.*, 2022, **306**, 102723.
36 Y.-H. Seo, I. H. Cho and S.-I. Na, *J. Alloys Compd.*, 2019, **797**, 1018–1024.
37 Y. Huang, Y. Li, E. L. Lim, T. Kong, Y. Zhang, J. Song, A. Hagfeldt and D. Bi, *J. Am. Chem. Soc.*, 2021, **143**, 3911–3917.
38 A. A. Zhumekenov, M. I. Saidaminov, M. A. Haque, E. Alarousu, S. P. Sarmah, B. Murali, I. Dursun, X.-H. Miao, A. L. Abdelhady, T. Wu, O. F. Mohammed and O. M. Bakr, *ACS Energy Lett.*, 2016, **1**, 32–37.
39 Y. Yang, C. Liu, Y. Ding, Z. Arain, S. Wang, X. Liu, T. Hayat, A. Alsaedi and S. Dai, *ACS Appl. Mater. Interfaces*, 2020, **12**, 49275.
40 X. Zhang, C. Liang, M. Sun, H. Zhang, C. Ji, Z. Guo, Y. Xu, F. Sun, Q. Song and Z. He, *Phys. Chem. Chem. Phys.*, 2018, **20**, 20732.
41 Z. Yang, Y. Zhang, G. Wu, S. Li, Z. He, M. Ou, H. Yuan, S. Li, H. Zhu, R. Yu and Z. a. Tan, *Adv. Mater.*, 2024, **36**, 10425.
42 Y. Wang, C. Duan, J. Li, W. Han, M. Zhao, L. Yao, Y. Wang, C. Yan and T. Jiu, *ACS Appl. Mater. Interfaces*, 2018, **10**, 20128–20135.
43 Q. Fan, Y. Wang, M. Zhang, B. Wu, X. Guo, Y. Jiang, W. Li, B. Guo, C. Ye, W. Su, J. Fang, X. Ou, F. Liu, Z. Wei, T. C. Sum, T. P. Russell and Y. Li, *Adv. Mater.*, 2018, **30**, 6.
44 D. Liu, Y. Wang, H. Xu, H. Zheng, T. Zhang, P. Zhang, F. Wang, J. Wu, Z. Wang, Z. Chen and S. Li, *Sol. RRL*, 2019, **3**, 04546.
45 J. Liu, Y. Guo, M. Zhu, Y. Li and X. Li, *J. Power Sources*, 2020, **476**, 228648.
46 J. Xu, J. Cui, S. Yang, Y. Han, X. Guo, Y. Che, D. Xu, C. Duan, W. Zhao, K. Guo, W. Ma, B. Xu, J. Yao, Z. Liu and S. Liu, *Nano–Micro Lett.*, 2022, **14**, 152–166.
47 D. Wang, M. Wright, N. K. Elumalai and A. Uddin, *Sol. Energy Mater. Sol. Cells*, 2016, **147**, 255–275.
48 S. Svanstrom, T. J. Jacobsson, G. Boschloo, E. M. J. Johansson, H. Rensmo and U. B. Cappel, *ACS Appl. Mater. Interfaces*, 2020, **12**, 7212–7221.
49 L. K. O. Yuichi Kato, M. V. Lee, S. Wang, S. R. Raga and Y. Qi, *Adv. Mater. Interfaces*, 2015, **2**, 00195.